Journal of Engineering Mathematics **47:** 1–16, 2003.

Numerical modelling of a surface-stress driven density-stratified fluid

DUNCAN E. FARROW[1] and CRAIG L. STEVENS[2]
[1]*Mathematics and Statistics, Murdoch University, Murdoch, WA 6150, Australia*
[2]*National Institute of Water & Atmospheric Research, PO Box 4-901, Kilbirnie, Wellington, New Zealand*

Received 22 june 2001; accepted in revised form 14 January 2003

Abstract. The initial response of a density-stratified fluid in a rectangular domain to a surface stress is modelled numerically. The model is laminar, two-dimensional and non-hydrostatic. Upwelling of deep fluid at the upwind end of the fluid is critical to the subsequent evolution of the stratification. It is confirmed that upwelling is a wave process and consideration of flow at the upwind end-wall illustrates the flow structure of partial upwelling. Numerically, to ensure adequate penetration of surface stress, an increased viscosity is needed. Comparisons are made between the present numerical results and previously published experimental observations.

Key words: internal waves, stratified flow, upwelling

1. Introduction

The interaction of one fluid flowing past a cavity filled with a second fluid has a range of applications in natural and built environments [1]. An example from geophysical fluid mechanics is the response of a density-stratified lake or reservoir to the initiation of a surface wind stress. Mortimer's classic laboratory experiments [2] represented a lake using a stratified wind-driven cavity. That work showed how large-amplitude internal deflections could control vertical mass transfer in a stratified cavity. Of particular interest is the upwelling of deeper water to the surface via basin scale internal waves generated by the wind stress [3]. The surface stress is then parametrized relative to the stability and horizontal scale of the fluid [3]. Subsequently this parameterization has been presented as the Wedderburn number [4]

$$W = \frac{g' h_1^2}{u_*^2 L}, \tag{1}$$

where h_1 and L are the average depth of the surface layer and the length of the basin respectively, $g' = g\Delta\rho/\rho_0$ is the reduced gravity, where g is the acceleration due to gravity, ρ_0 is a reference density and $\Delta\rho$ is the density change across the interface. A value of $W < 1$ indicates upwelling whereby the lower layer reaches the surface at the upwind end of the fluid. Related experimental work more clearly defined the behaviour and parameterization [5] and the transient response of the upwelling [6].

The present paper presents a numerical approach to identifying a number of facets of upwelling. It uses the laboratory experiments of [6] as inspiration and validation and then examines the upwind end wall flow behaviour specifically in the context of the upwelling process. Those experiments used a three-layered fluid and generated the stress with a moving belt floating on the surface. The subsequent fluid response was a combination of internal waves,

circulation and turbulence, where the end-walls caused horizontal pressure gradients which resulted in longitudinal gradients in density structure. The magnitude of this density gradient, which is effectively a density interface slope, is related to the balance between the force due to the wind and the opposing force generated by the baroclinic gradient. The interface slopes are described in terms of the lake number L_N [6] which balances moments generated by these forces and is conceptually an integral Wedderburn number [5]. This parameter was introduced to handle variable bathymetry and stratification and is defined by [7]

$$L_N = \frac{M_{bc}}{\tau A z_v}, \tag{2}$$

where M_{bc} is the baroclinic moment about the centre of volume of the water column if the density structure were tilted at a constant slope at the point of upwelling, A is the surface area of the cavity, τ is the surface shear stress and z_v is the distance from the water surface to the centre of volume.

The timescale for this inherently transient process is the period of the first horizontal mode internal seiche given by

$$T_1 = \frac{2L}{c_p}, \tag{3}$$

where $c_p \sim \sqrt{g'H}$ is the phase speed of the wave and H is the average depth, L is the length of the basin and $g' = g\Delta\rho/\rho_0$ is the reduced gravity. A combination of isotherm tilt at equilibrium, as described by L_N, and duration of the forcing relative to T_1 defines the expected dynamics [8]. Monismith [5] identified that upwelling could occur even when the parameterization suggested it would not. This was termed partial upwelling and was localised near the upwind endwall and is not easily quantified with laboratory experiments designed to elucidate the flow development in the basin as a whole.

The modelling approach described here uses a laminar, uniform viscosity model to capture the essential basin-scale dynamics that lead to upwelling. The validity of this approximate approach and the conclusions drawn are considered in the discussion. The new work presented here seeks to (i) validate a model for small cavities that captures the basin scale dynamics critical to upwelling, (ii) identify the nature and timescale of partial upwelling and (iii) pay particular attention to kinematics at the endwall. The present work is not aimed at modelling the response after upwelling has occurred. In the following sections we describe the numerical method, the results of the simulations and then discuss their relevance to the overall problem.

2. Numerical modelling

2.1. Model formulation

The response of a stratified fluid to a surface stress have previously been studied using a cloud-in-cell approach [9], a buoyancy-extended k-ε closure approach [10] and a two-dimensional eddy-viscosity model [11]. Some of these studies [10, 11] model the experiments of [5]. The buoyancy-extended k-ε closure approach [10] led to an apparent over-estimation of the entrainment at the downwind end. Other work [12] uses an approach similar to the present work when modelling the experimental results of [13]. However, the belt velocities were smaller than those used here and they used a cavity that had an aspect ratio closer to unity.

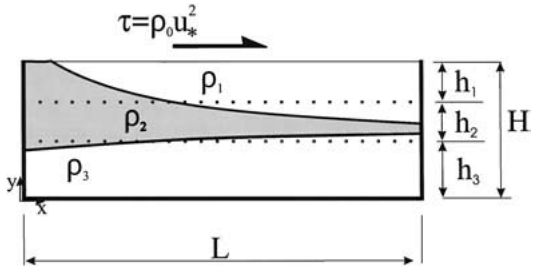

Figure 1. Schematic of a rectangular stress-driven domain containing a three layer fluid.

In the experiments of [6] and [5], the surface stress induced a narrow jet of fluid at the surface that would turn downward at the downwind end wall and erode the underlying stratification. In terms of modelling a lake, this jet is an artefact of introducing the stress at the laboratory scale. In the laboratory experiments a panel of porous matting was introduced to absorb the momentum of the jet. A similar jet-like structure occurs in the numerical results with a similar effect on the stratification. In fact, when the jet strikes the downwind wall, the numerical model is not able to adequately resolve the subsequent flow. To overcome this a linear drag term $\lambda\mathbf{u}$ (where $\mathbf{u} = (u, v)$ is the fluid velocity) is introduced into the momentum equations with $\lambda \neq 0$ only in some region close to the downwind endwall (a sponge layer). The magnitude of λ is increased linearly from zero at the beginning of the end flow region to $\lambda_{\max}$ at the end wall $x = L$. That is

$$\lambda(x) = \begin{cases} 0, & 0 < x < x_\lambda \\ \lambda_{\max}(x - x_\lambda)/(L - x_\lambda), & x_\lambda < x < L. \end{cases} \tag{4}$$

The choice of the damping parameter $\lambda_{\max}$ will be discussed later. Suffice for now that for all simulations $x_\lambda = 0{\cdot}936L$. This makes the sponge layer in the numerics marginally thicker than the diffuser used in the experiments. However, it was found that a thicker, more gradual damping was most effective in the numerical model for absorbing momentum without adding significantly to computational expense. In any case, the numerical results show that the flow at the upwind end (where upwelling occurs) is insensitive to moderate changes in x_λ.

The response of a stratified water body to a surface wind stress is modelled by the flow of a fluid in a two dimensional rectangular domain (Figure 1). The equations of motion used in this work are

$$\frac{\mathrm{D}u}{\mathrm{D}t} + \lambda u = -\frac{1}{\rho_0}\frac{\partial p}{\partial x} + \nu\nabla^2 u, \tag{5}$$

$$\frac{\mathrm{D}v}{\mathrm{D}t} + \lambda v = -\frac{1}{\rho_0}\frac{\partial p}{\partial y} + \nu\nabla^2 v - g', \tag{6}$$

$$\frac{\mathrm{D}\rho}{\mathrm{D}t} = \kappa\nabla^2\rho, \tag{7}$$

$$\frac{\partial u}{\partial x} + \frac{\partial v}{\partial y} = 0, \tag{8}$$

where u and v are the fluid velocities in the x- and y-directions respectively, p is the perturbation pressure, ρ is the density, ρ_0 is the reference density, ν is the (constant and uniform)

kinematic viscosity and κ is the diffusivity of the stratifying species which is taken to be salt (as it was in the experiments of [6]). In the above equations, the Boussinesq assumption has been made, $\mathrm{D}(.)/\mathrm{D}t$ is the material derivative $(\frac{\partial}{\partial t} + \mathbf{u} \cdot \nabla)$ and ∇^2 is the two-dimensional Laplacian operator. The boundary and initial conditions on the flow are

$$\rho_0 \nu \frac{\partial u}{\partial y} = \tau f(x,t) = \rho_0 u_*^2 f(x,t) \quad \text{on} \quad y = H, \tag{9}$$

$$v = 0, \quad \frac{\partial \rho}{\partial y} = 0 \quad \text{on} \quad y = H, \tag{10}$$

$$u = v = \frac{\partial \rho}{\partial y} = 0 \quad \text{on} \quad y = 0, \tag{11}$$

$$u = v = 0, \frac{\partial \rho}{\partial x} = 0 \quad \text{on} \quad x = 0,\ L, \tag{12}$$

$$u = v = 0,\ \rho = \rho_{\text{init}}(y) \quad \text{at} \quad t = 0. \tag{13}$$

where τ is the surface stress, u_* is the friction velocity and $f(x,t)$ is a surface stress modulation function chosen to mimic experimental parameters. The surface stress rather than the surface velocity is specified here as it is the stress that is generally used in the scaling for the problem. Also, it is the surface stress that is measured in [6].

The initial stratification $\rho_{\text{init}}(y)$ shown in Figure 1 needs to be specified. Following [6] a three layer stratification is used to provide the density interface (the 'thermocline' in a stratified lake) with its own identifiable region, that is

$$\rho_{\text{init}}(y) = \begin{cases} \rho_1 & h_2 + h_3 < y \le H \\ \rho_2 & h_3 < y \le h_2 + h_3 \\ \rho_3 & 0 \le y \le h_3 \end{cases}, \tag{14}$$

where $h_1 + h_2 + h_3 = H$. In practice, the sharp density interfaces inherent in (14) cause numerical difficulties. Consequently, in the simulations the initial density step between adjacent layers is smoothed over a few grid points. This smoothing is done using the formula $\rho_{ij}^{\text{new}} = (\rho_{ij-1}^{\text{old}} + 2\rho_{ij}^{\text{old}} + \rho_{ij+1}^{\text{old}})/4$ where ρ_{ij} is the density at the point (x_i, y_j). This smoothing is performed twice so that the change in density between adjacent layers occurs over five gridpoints (about 10 mm) which is significantly less than the layer thicknesses (30 mm to 75 mm). This has an effect similar to molecular diffusion in the laboratory experiments over the period between filling and the commencement of surface stress.

The surface stress that drives the flow in the cavity varies both with time and space, as implied by the notation used in (9). Following [6], the stress is linearly ramped from $t = 0$ up to its maximum value after which it is held constant for the duration of the simulation. The stress is also a piece-wise linear function of x so that the stress vanishes at either end of the cavity. This is to avoid vigorous corner flow and to reflect the fact that the stress is applied to a limited area in the experiments of [6]. Thus, the stress modulation function $f(x,t)$ has the general form $f = F(x)G(t)$ where

$$F(x) = \begin{cases} x/x_1 & 0 \le x \le x_1 \\ 1 & x_1 < x \le x_2 \\ (x - L)/(x_2 - L), & x_2 < x \le L \end{cases} \tag{15}$$

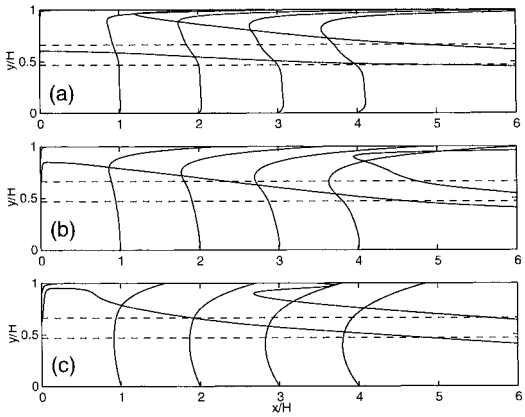

Figure 2. Plots of numerical results showing density interface positions and selected horizontal velocity profiles (not to scale) at $t/T_1 = 0{\cdot}52$ for three different values of viscosity applied to experiment E2. These values are (a) 7, (b) 35 and (c) 175 times the molecular value. The dashed lines are the interface positions at $t = 0$.

and

$$G(t) = \begin{cases} t/t_1 & 0 \leq t \leq t_1 \\ 1 & t_1 < t \end{cases} . \tag{16}$$

In the present work (except where stated otherwise), $t_1 = T_1/2$, comparable to [6]. Also, for all simulations $x_1 = 0{\cdot}05L$ and $x_2 = 0{\cdot}915L$. Note that the stress is assumed to be constant for $x_1 < x < x_2$. The stress distribution for [6] is not known, only the integrated stress is measured. In the absence of detailed knowledge of the stress distribution a uniform stress distribution is appropriate.

The role of viscosity in the present results needs to be addressed. The laboratory flows of [6] generated turbulence and significant mixing almost as soon as the surface stress was initiated. The experimental results of [6] suggest that mixing does not have a dominant effect on the processes leading to upwelling but that the degree of upwelling has a large effect on the longer-term mixing. Consequently, a laminar, uniform viscosity model is used here to model the flow until upwelling occurs. There is one aspect, however, where turbulence is important for the initiation of upwelling. The near-belt turbulence transports the surface stress down into the body of the upper layer achieving a greater stress penetration than for laminar flow. It has been demonstrated that stress penetration is determined by both the equilibrium density interface tilt and the internal wave field [14, 15]. Stress penetration is achieved in the present work by using a uniform value for ν approximately 35 times higher than the molecular value. For this value of ν, the viscous boundary layers that form at the top and bottom of the cavity are thinner than the density layers, at least until upwelling occurs. However, the upper viscous boundary layer is sufficiently thick to transport the surface stress into the body of the upper layer which is a more accurate representation of the experiments of [6].

Figure 2 shows numerical density and velocity structure at the upwind end of the tank for three different values of ν (7, 35 and 175 times the molecular value). This figure corresponds to experiment E2 of [6] (see later) at a time $t/T_1 = 0{\cdot}52$ just after upwelling has occurred. In Figure 2(a), where ν is 7 times the molecular value, the surface stress has not penetrated sufficiently into the upper layer compared with the experimental results and upwelling has been delayed compared with the corresponding experimental results. Also, (not shown in

Table 1. Experimental variables and parameters. The total depth of the fluid H for both experiments was 160mm, the individual layer depths are h_1, h_2 and h_3 from top to bottom (see Figure 1). The other parameters are $\varepsilon_{ij} = (\rho_j - \rho_i)/\rho_0$, T_1 and T_2 are the first and second internal mode periods respectively, u_*^2 is the friction velocity and L_N is the lake number defined in the text.

Experiment	h_1 (mm)	h_2 (mm)	h_3 (mm)	ε_{12} ($\times 10^3$)	ε_{23} ($\times 10^3$)	T_1 (s)	T_2 (s)	u_*^2 $(\mathrm{ms}^{-1})^2(\times 10^4)$	L_N
E6	67	42	51	3·14	3·60	86	167	0·84	2·90
E2	54	31	75	1·85	3·61	90	224	4·00	0·35

Figure 2(a)) the flow at the downwind end has become unstable, signifying the onset of turbulence and thus is not adequately resolved by this model. Essentially, the stress is driving a recirculating flow in the upper layer. The middle panel of Figure 2 (ν is 35 times the molecular value) has the best correspondence with the experimental data. This value of ν provides sufficient penetration of the surface stress into the upper layer without damping out the wave response. For Figure 2(c) (ν is 175 times the molecular value), the viscous boundary layer has grown too thick and occupies nearly the whole upper layer. This value of ν leads to a damping of the wave response of the flow and the velocity profiles are close to those associated with buoyancy free flow. In practice, there is a wide range of values for ν (approximately 15 to 100 times the molecular value), where experimental and numerical results are in good agreement. In the following results, $\nu = 3{\cdot}5 \times 10^{-5}$ and $\kappa = 9{\cdot}2 \times 10^{-8}$ (which is about 35 times the molecular value for salt). Note that $\nu/\kappa \approx 381$ so there is very little diffusion of the stratifying species for the duration of the numerical experiments considered here. This is desirable since the focus here is on the wave response leading to upwelling. Having a large κ would lead to significant thickening of density interfaces which complicates the dynamics.

2.2. NUMERICAL SOLUTION

The system of equations and the associated boundary conditions are solved numerically using the numerical scheme developed by Armfield [16]. This is a SIMPLE type scheme [17, pp. 126–131] applied on a non-staggered mesh; that is, all variables (velocities, pressure and density) are stored at the same grid point which lies at the centre of its control volume. Additionally, Leonard's [18] QUICK scheme is used for the advection terms and time integration is performed using the ADI method [19].

The experiments of [6] used a 1880 mm $\times$ 160 mm rectangular tank. A non-uniform discretization is used to ensure adequate resolution of the boundary layers that form near solid boundaries. Errors associated with changing the grid scale are kept small by ensuring that the size of neighbouring grid boxes differ by no more than 5%. In the fine resolution simulations discussed below, a 186×70 grid is used with Δx ranging from 1 mm near the wall to 45 mm in the centre of the flow domain and Δy ranging from 1·5 mm to 4·5 mm. There is a diffusion of momentum stability constraint on the time step $\Delta t < \Delta x^2/4\nu \approx 7 \times 10^{-3}$s. This constraint is conservatively met by $\Delta t = 4 \times 10^{-3}$s so a total of approximately 5×10^5 time steps are required for each simulation.

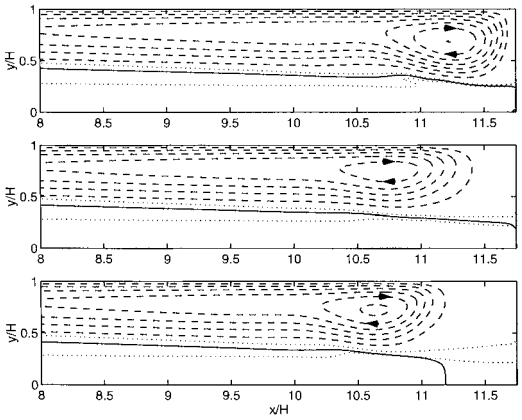

Figure 3. Plots of density and streamfunction fields at $t/T_1 = 0{\cdot}8$ at the downwind end for three simulations of E6 with different values for the end region damping parameter $\lambda_{\max}$. They are (a) $\lambda_{\max} = 0$, (b) $\lambda_{\max} = 2{\cdot}9\text{s}^{-1}$ and (c) $\lambda_{\max} = 11{\cdot}5\text{s}^{-1}$. The dashed contours are the streamfunction with the solid contour being the zero contour. The dotted lines are density interface positions.

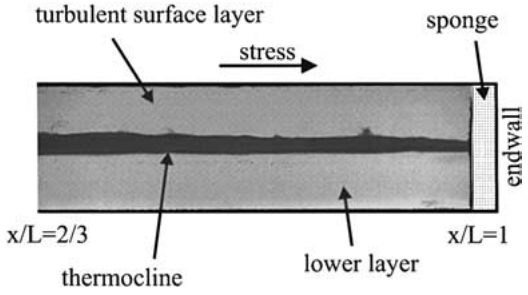

Figure 4. A photograph from the laboratory experiments detailed in [6] showing interfacial details similar to that plotted in Figure 3.

3. Results

Two experimental configurations from [6] are discussed here. The first (labelled E6 in [6]) represents the wave response ($L_N = 2{\cdot}9$) of the stratified fluid to the wind stress. In this case, upwelling is not expected to occur. The second configuration (labelled E2 in [6]) has a $L_N = 0{\cdot}35$ so upwelling of the middle layer is expected. The experimental parameters are summarised in Table 1. Note that all simulations are done using a non-dimensionalised system. However, to maintain the strong link between the present results and those of [6], all parameters are given in dimensional terms.

Before going on to describe the results in detail, a value for the damping parameter $\lambda_{\max}$ needs to be chosen. Figure 3 shows the density and streamfunction fields in the downwind end region of the computational domain for three simulations of E6 with increasing values for the damping parameter $\lambda_{\max}$. For $\lambda_{\max} = 0$, the flow in the end region is very vigorous with much disruption to the density structure. In particular, there is a folding over of the lower interface near $x/H = 11$. Note that many of the features observed for $\lambda_{\max} = 0$ are likely to be unphysical as the numerical model does not adequately resolve the flow. However, the general response is comparable to unpublished experiments preliminary to [6] without downwind damping. For $\lambda_{\max} = 11{\cdot}5$ (Figure 3(c)), the flow is over-damped relative to the experiments. The damped region is acting like a solid wall with the surface jet being turned downwards before it has penetrated into the end region. In Figure 3(b) where $\lambda_{\max} = 2{\cdot}9$ (the value used in the simulations in this work), the damping is not so strong as to suppress the vertical motion associated with the wave response but is strong enough to absorb much of the momentum of the surface jet. Figure 4 shows a photograph of an experiment similar to E6 from [6] at approximately the same time as the results in Figure 3. The middle layer is marked

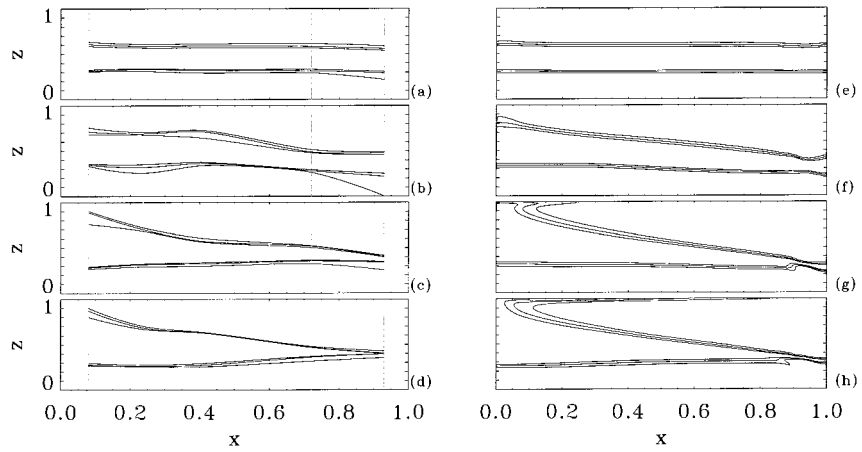

Figure 5. A series of snapshots of the interface positions from the experimental results of E6 of [6] (a–d) with corresponding numerical results (e–h). The non-dimensional times are $t/T_1 =$ (a, e) 0·19, (b, f) 0·58, (c, g) 0·97 and (d, h) 1·35.

with dye. The agreement between the laboratory and numerical density structure in the end region suggests that setting $\lambda_{\max} = 2{\cdot}9$ is appropriate. In any case, these and other numerical experiments show that, up until the time that upwelling occurs, the flow structure near $x = 0$ where upwelling occurs depends only weakly on $\lambda_{\max}$.

3.1. THE WAVE RESPONSE: E6

In this $L_N = 2{\cdot}9$ experiment, upwelling is not expected to occur. Figure 5 shows sequences of snapshots of density contours from both the experimental and numerical results at corresponding times. The density contours are chosen to reflect the positions of the two interfaces and the neighbouring contours give an indication of their thicknesses. The data from the laboratory and numerics are contoured differently, otherwise information is lost. The numerical results are sufficiently well resolved so as to contour directly. The laboratory contoured by using a spline interpolation for each isopycnal, this avoids the difficulty of two-dimensional interpolation where there is a large variation in horizontal versus vertical resolution. The experiments are salt stratified. In fact, over the time scales considered here, there is virtually no diffusion of salt so the thickening of the interfaces is mainly due to a locally diverging velocity field.

Despite the lack of knowledge of the exact laboratory boundary conditions the two sets of results are in reasonable agreement both in overall appearance and in many of the details. The numerical results have captured the downwind compression of the middle layer which is indicative of the second mode response. There appears to be a transient discrepancy between the results at $t/T_1 = 0{\cdot}58$ (panels (b) and (f)) with the experimental results showing more short wavelength wave motion and consequent distortion of density interfaces. The discrepancy is short-lived as the numerical and experimental results are in much better agreement for later times. In particular, the interfacial tilts compare well (see later) and the increasing steepness of the upper interface near the upwind end is present in both sets of results. Also, the finer details of the density structure (for example the thickening and thinning of the density interfaces bounding the middle layer) are in good agreement.

Figure 6 shows a comparison of the evolution of the density and horizontal velocity profiles at $x = L/3$ as a function of time. The fluid velocities in the experimental results are 15%–20%

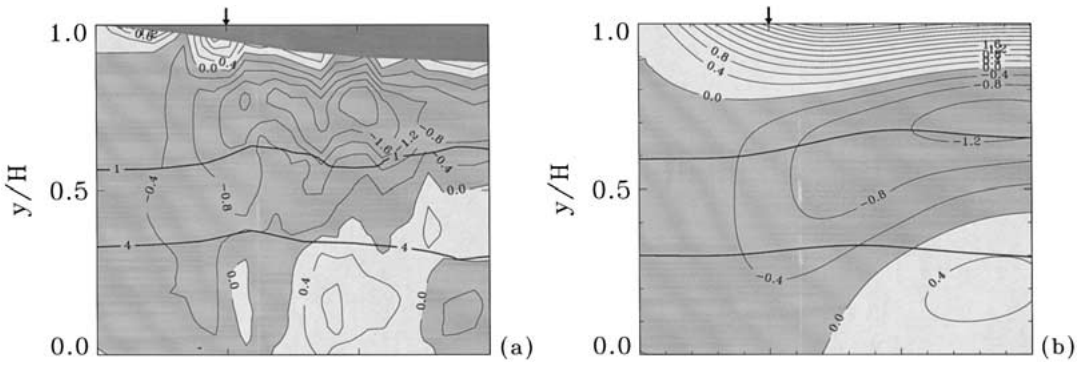

Figure 6. Velocity contours for E6 as a function of depth and time at $x/L = 1/3$ for (a) the laboratory results and (b) the numerical equivalent. The density interfaces are superimposed as thick lines and the solid arrow at $t/T_1 = 0{\cdot}5$ indicates the ramping time for the surface stress.

larger than those from the numerical results. The reason for this is not clear but it could be due a mismatch in the distribution of the surface stress, a difference in the thickness of the surface boundary layer, the enhanced viscosity used in the numerical model or the degree or nature of damping at the downwind end. One feature of the experimental results that has been captured in the numerical results quite accurately is the position of the $u = 0$ contour. The presence of this contour is an indicator of the wave response. In both figures, this emerges from $y = 0$ at $t/T_1 \approx 0{\cdot}7$. In the experimental results the contour is at $y/H \approx 0{\cdot}5$ at $t/T_1 = 1{\cdot}3$ while in the numerical results it is at $y/H \approx 0{\cdot}4$. There are other features where the two sets of results differ, particularly the changes of sign of u in the lower layer at $t/T_1 \approx 0{\cdot}6$ and $t/T_1 \approx 1{\cdot}4$.

Note that the $L_N = 2{\cdot}9$ parameterization indicates that upwelling is not expected to occur in this experiment. However, the numerical results (see Figure 5(f)) show interfacial fluid at the surface at the upwind end. The experimental results may potentially be upwelling, however, as data could not be recorded very close to the endwall or belt, this could not be confirmed.

3.2. THE UPWELLING RESPONSE: E2

In this $L_N = 0{\cdot}35$ experiment upwelling is expected to occur. This value for L_N is at the lower end of the relevant range of values and represents a very vigorous response. As well as the enhanced baroclinic tilt, the laboratory version of E2 is distinguished from E6 by the presence of strong turbulent mixing of the density structure. In fact, the vertical mixing occurs on a similar time-scale to the wave/upwelling response so that the middle layer loses much of its identity at the upwind end before the wave response can generate upwelling. Subsequent to this, the lower interface continues to rise at the upwind end and upwells. This has consequences for the comparison between the experimental and numerical results as there is no parameterization of mixing other than the increased viscosity and diffusivity in the model. However, the numerical and experimental results are in reasonable agreement until the time that the middle layer in the laboratory loses its identity through vertical mixing (at $t/T_1 \approx 0{\cdot}3$).

Figure 7 shows a number of snapshots of the density field for E2 from both the experimental and numerical results. As expected, the earlier two times are in reasonable agreement (up to the time that upwelling occurs) but for later times, there is considerable discrepancy. The influence of turbulent mixing is evident in the experimental results as the middle layer is mixing with the upper layer fluid and thickening as a result. For $t/T_1 > 1{\cdot}1$ in the experimental results, the upper two layers are sufficiently mixed as to be considered homogeneous.

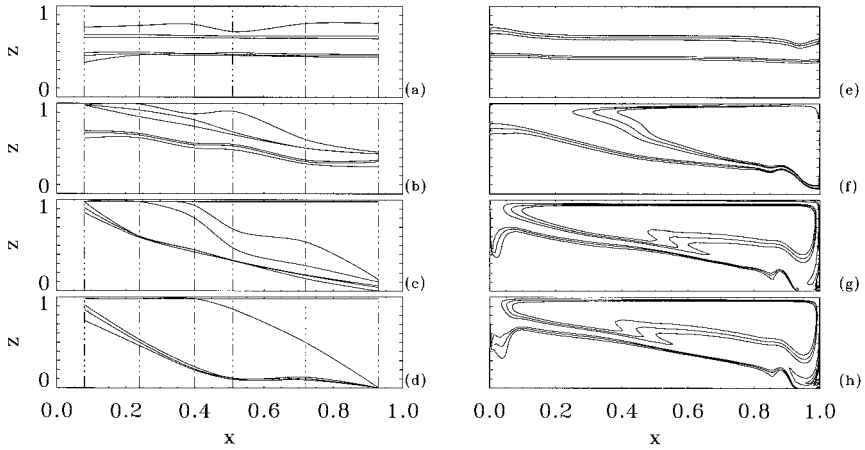

Figure 7. A series of snapshots of the interface positions from the experimental results of E2 of [6] (a–d) with corresponding numerical results (e–h). The non-dimensional times are t/T_1 = (a, e) 0·16, (b, f) 0·48, (c, g) 0·8 and (d, h) 1·11.

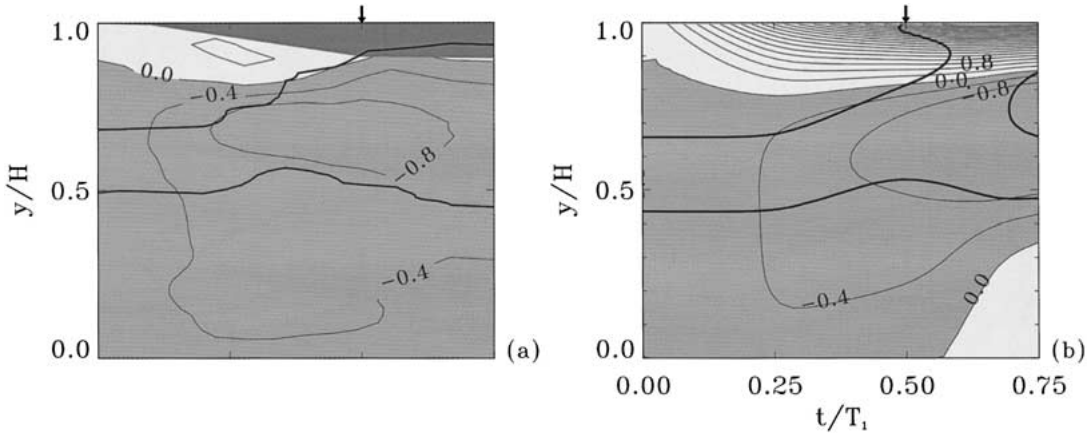

Figure 8. Velocity contours for E2 as a function of depth and time at $x/L = 1/3$ for (a) the laboratory results and (b) the numerical equivalent. The density interfaces are superimposed as thick lines and the solid arrow at $t/T_1 = 0{\cdot}5$ indicates the ramping time for the surface stress.

After this time, the response is more accurately described as that of a two layer fluid. In the numerical results, no such mixing occurs and as the middle layer is upwelled, it is carried downwind by the surface jet before recirculating in the upper layer. This recirculation can be seen in figures 7(g) and (h) where the recirculating fluid forms a tongue of fluid advected to the left above the middle layer. In fact, when this tongue of fluid emerges from the right of the cavity, the upper layer is entirely surrounded by middle layer fluid. Note that the experimental contours from [6] are of equilibrium density sorted profiles which has the effect of eliminating density overturns that occurred in their experiments. Since their analysis relies on layer averaging this sorting has no effect on their interpretation. An instantaneous snapshot might well be closer to the numerical results.

Figure 8 shows the evolution of the E2 density and horizontal velocity profiles at $x = L/3$ with increasing time. This shows the dramatic effect that vertical mixing has on the flow development in the experimental results. For times up to $t/T_1 \approx 0{\cdot}3$ the two sets of

. Average interface slopes for experimental and numerical results for E6 at times corresponding to Figure 5. Each slope is multiplied by 10^2.

	t/T_1	0·19	0·58	0·97	1·35
upper	exp.	−0·379	−2·69	−4·32	−4·41
	num.	−0·0731	−2·89	−4·77	−4·48
lower	exp.	−0·262	−1·22	0·599	1·38
	num.	−0·0313	−1·32	−0·535	0·625

. Average interface slopes for experimental and numerical results for E2 at times corresponding to figure 5. Each slope is multiplied by 10^2. The entry $(*)$ corresponds to a time when there is no clearly identifiable upper interface.

	t/T_1	0·16	0·48	0·80	1·1
upper	exp.	−0·143	−5·91	−8·71	$(*)$
	num.	−0·154	−11·4	−2·10	−1·43
lower	exp.	−0·0948	−3·64	−8·38	−7·95
	num.	−0·125	−5·30	−4·26	−4·99

results are in good agreement both in the overall structure and the details of the velocity field. As discussed earlier, mixing now takes over as the dominant process in the upper two layers in the experimental results, leading to significant differences between the numerical and experimental results. In the experimental results, mixing is so dominant that the interface between the upper and middle layers is eroded before upwelling can occur. This does not occur in the numerical results where the wave response continues to develop up to and beyond middle layer upwelling, which occurs at $t/T_1 \approx 0{\cdot}34$. The difference in the wave response between the two sets of results is apparent in the position of the $u = 0$ contour in Figure 8. In the experimental results, the contour emerges from the bottom $y = 0$ at $t/T_1 \approx 1{\cdot}0$ (not visible in Figure 8) whereas it appears earlier at $t/T_1 \approx 0{\cdot}6$ in the numerical results. Note also that the recirculation velocities in the upper layer of the numerical results are two to four times larger than those in the experimental results after $t/T_1 \approx 0{\cdot}3$. This is presumably because much of the energy input from the belt is being dissipated in the turbulence rather than feeding into the kinetic energy of the recirculating flow. This dissipation also leads to the later wave response in the experimental results mentioned earlier.

4. Discussion

4.1. Effectiveness of numerical model

Prior to upwelling, the present numerical results are generally in reasonable agreement with the experimental results. It is only after upwelling that the lack of turbulent mixing in the numerical simulations leads to significant differences in the density structures. This is particularly the case for the experimental results for E2 where vertical mixing significantly erodes the

stratification before full upwelling can occur. Tables 2 and 3 provide a quantitative comparison between the experimental and numerical results. Here, the average slopes of the two layer interfaces are calculated for the times shown in Figures 5 and 7. For the numerical results only data for $0{\cdot}25 < x/L < 0{\cdot}75$ is included to remove localised endwall effects. For E6 (Table 2), the numerical results predict the experimental upper interface slope very well. The largest discrepancy occurs early at $t/T_1 = 0{\cdot}19$. This could be a reflection of the relatively fast turbulent transport of stress in the experiments compared with the laminar numerical results. The agreement for the lower interface is not as good. Specifically, the change in sign of the slope of the lower interface is delayed in the numerical results when compared with the experimental results. For E2 (Table 3), the agreement between the experimental and numerical results is not as close due mainly the mixing mentioned above. By $t/T_1 = 1{\cdot}1$ the upper interface has disappeared. The slope of the bottom interface from the numerical results is about half that of the experimental results for most of the simulation.

Another effect of the highly turbulent upper layer in the experiments is the generation of significant short wavelength waviness in the lower layers via pressure perturbations associated with the larger scale eddies in the upper layer. These eddies are absent in the numerical results as is the consequent waviness in the lower layers (for example, compare Figures 5(b) and (f)). This extra waviness in the experimental results does not have a significant effect on the upwelling process which is dominated by basin scale motions. Closer examination of the experimental results indicate that the waviness is due to the recirculation of turbulent fluid in the upper layer associated with the moving belt. The recirculating turbulent fluid is absent in the numerical results as it has been slowed by the sponge layer. This recirculation of turbulent fluid is also responsible for the extra waviness in the experimental results evident in Figure 6(a) and also in Figure 5(b). The absence of the extra waviness in the numerical results is considered to be secondary as far as modelling the upwelling process is concerned as it may perturb the upwelling but not significantly retard it.

A further distinction between the two sets of results is that the surface velocity in the numerical results is not constant with x. Besides the adjustment at each end to satisfy the boundary conditions, u at $y = H$ is increasing with x. This is a reflection of the fact that the viscous boundary layer thickens as it is carried along by the belt. To maintain the uniform stress boundary condition, the surface velocity increases to maintain the requisite velocity gradient at the surface. It is possible to get around this by changing the upper boundary condition to a fixed slip velocity condition. However, the surface stress cannot then be specified as an input to the model. It is the surface stress measurements from [6] that form a fundamental part of the model specification.

The general conclusion is that, other than the mixing, the dynamic structure of the two models are in good agreement and are representative of the experimental results up until the time upwelling occurs.

4.2. The initiation of the stress

The stress initiation differs between the experimental and numerical results. In the experimental results, the belt induces a turbulent boundary layer that transports stress into the upper layer. In the numerical results where turbulence is not directly modelled, the flow develops a moving viscous boundary layer at the surface associated with the belt. In either case, the boundary layers entrain fluid from the upwind end of the interior of the domain, which feels the boundary layer as a distributed sink at the upwind end and a distributed source at the

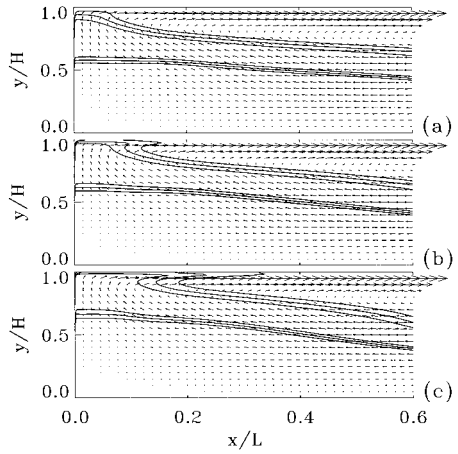

Figure 9. A series of snapshots of the velocity field at the upwind end as upwelling occurs for the numerical simulation of E2. The times are $t/T_1 =$ (a) 0·3, (b) 0·34 and (c) 0·39.

downwind end. The interior flow is potential until there is a significant deflection of the density interfaces to lead to the baroclinic generation of vorticity. Thus at small times, the flow in the interior of the domain is a plug flow towards the upwind end. This interior velocity structure is apparent in both the experimental and numerical results (see Figures 6 and 8) and persists up to $t/T_1 \approx 0{\cdot}5$ for E6 and $t/T_1 \approx 0{\cdot}3$ for E2. The interior recirculation velocity for E2 is of the order of 1 to 2 cm s^{-1} which leads to a recirculation time of the order of approximately T_1, that is, longer than the upwelling time of $0{\cdot}34T_1$. After these times, the flow in the lower layer starts to decelerate as the wave response of the interior flow begins due to the relaxation of the initial tilt.

4.3. THE UPWELLING PROCESS

Figure 9 shows three density and velocity structure plots at the upwind end at different times from the numerical results of E2 during upwelling (which occurred at $t/T_1 \approx 0{\cdot}34$). Note that the velocity vectors shown in that figure are interpolated from the calculations for clarity. Also, the vectors at the surface $y = H$ have been omitted since they are much larger and would dominate the figure. The velocity structure does not change significantly over the three plots. The wave response has commenced with the flow near the bottom at the upwind end about to reverse (see Figure 8(b)). Also, the vertical velocities are largest in the region between $x = 0$ and $x \approx 0{\cdot}1L$. This region of large vertical velocities extends from near the surface to $y/H \approx 0{\cdot}7$ and in this region there is enhanced upwelling in the sense that the slope of the interfacial deflections is larger than those at greater x. Monismith [5] differentiates, for a two layer fluid, between total and partial upwelling. Total upwelling is the classical picture of upwelling when $L_N < 1$ (Wedderburn number in [5]) and the interface is bodily tilted. Partial upwelling occurs when $L_N > 1$ and the upper-most interfacial fluid is brought to the surface via circulation rather than seiche processes. This effect is encountered because of the diffuse interfaces that evolve through diffusion in the laboratory [5].

This effect is enhanced in the present work since a substantial middle layer is explicitly included in the model. Natural situations will typically be more complex as it is common for multiple remnant thermoclines to exist. Consequently pressure-driven flows at the upwind endwall will often have only very small buoyancy forces to counteract in order to bring denser

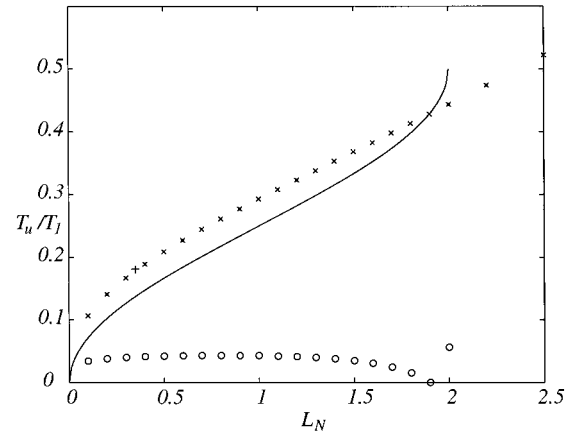

Figure 10. Upwelling time versus L_N based on coarse resolution simulations. The solid line represents the analytic expected time given by (17). The $\times$'s are numerical observations based on E2 for different surface stresses. The circles are the absolute difference between these two times. The $+$ at $L_N = 0{\cdot}35$ is the upwelling time for E2 using the fine resolution results.

fluid to the surface. This is also evident in Figures 5 and 7. Thus upwelling, in the broadest sense, occurs earlier than would be predicted by consideration of the slope in the interior of the domain. For example, the numerical results for E6 show that partial upwelling does occur though it is not expected to on the basis of the large value for L_N. The larger vertical velocities near the upwind wall occur because the flow there is not geometrically constrained by the local depth. If the bathymetry were shoaling there, the vertical velocities in the interior of the domain would be smaller and upwelling would presumably be weaker. This point is considered again later. In Figure 9(a) ($t/T_1 = 0{\cdot}3$), the middle layer fluid is just about to upwell. Note that the upper interface is in a region where the vertical velocity is increasing with y which gives rise to the thickening of the interface there. In Figure 9(b), fluid from the middle layer is being entrained into the surface jet and it is at this time that upwelling is occurring. Note that the structure of the density contours suggest that the middle of the jet (that is away from the surface) is moving faster than the surface fluid. This is not the case, rather the upwelling velocities slow dramatically near the surface to satisfy the boundary condition there which leads to a delay in the middle layer fluid reaching the surface. Once it has reached the surface, the faster velocities there eventually lead to the upwelled middle layer fluid at the surface catching up with the earlier entrained fluid leading to the 'folding over' of the isopycnals, which can be seen in Figure 9(c).

4.4. UPWELLING TIMESCALE

An analytic timescale was proposed for upwelling T_u given by [6]

$$T_u = \frac{T_1}{2\pi} \cos^{-1}(1 - L_N). \tag{17}$$

Figure 10 shows a comparison between the above timescale and a number of coarse resolution simulations for different L_N. These simulations were run on a 138×46 grid with a time step of $1{\cdot}6 \times 10^{-2}$s. This resolution is sufficient for determining upwelling times. Figure 10 includes one upwelling time based on a fine resolution run for E2 which agrees with the coarse resolution results. For Figure 10, the surface stress is applied instantaneously rather than ramped

as for the results discussed previously. This is because the derivation of the timescale given by (17) assumes an instantaneously applied stress. For the purposes of Figure 10, upwelling is defined to have occurred when fluid of density equal to the average of the upper two layers has arrived at the point $(x, y) = (0{\cdot}05L, 0{\cdot}98H)$, that is near the surface and one twentieth of the distance from the upwind end. It turns out in practice that the upwelling time determined from the numerical results is fairly insensitive to how it is defined so long as the point chosen to measure the density is inside the surface jet and outside the viscous boundary layer that forms at the vertical wall at $x = 0$.

Given that the estimate (17) is based on a linear approximation with simple first mode dynamics, the agreement between that estimate and the numerical results is good for $0{\cdot}25 < L_N < 1{\cdot}75$. Note that the numerical results capture the cusp-like curvature for small L_N. For L_N near 2, there is a difference between the behaviour of the two results as the estimate above predicts no upwelling for $L_N > 2$ while in the numerical results upwelling still occurs. In fact, upwelling occurs up to at least $L_N = 2{\cdot}5$. For this larger value of L_N, the upwelling is due to the general circulation and wall effects combined with the presence of a discrete middle layer. The partial upwelling is not due to the second mode response mentioned earlier since this takes longer to develop [6]. For smaller L_N, the upwelling is largely a first mode process so the numerical results and the estimate above track reasonably well. The circles in Figure 10 denote the absolute difference between the two sets of results. They are included here because the difference between the predicted upwelling time and the observed upwelling time is remarkably constant for $0{\cdot}1 < L_N < 1{\cdot}5$. It is not clear why this should be the case. Slight changes to the definition above for when upwelling occurs in the numerical results does not alter this property.

5. Conclusions

This paper considered a two-dimensional laminar constant viscosity model of the surface stress driven upwelling process in a density stratified cavity. The modelling here is restricted to the pre-upwelling regime. Once upwelling has occurred and vigorous mixing begins, the laminar model considered here does not resolve all the important features of the flow. A sponge layer at the downwind end of the fluid adequately managed the surface-driven jet that confounded earlier studies.

Both small and large lake numbers (L_N) have been considered and, despite the numerical simplifications, it was demonstrated that the model did match laboratory experiments within the limitations described above. The model was then used to explore the timing for the onset of upwelling. The first order model for this time proved adequate.

As to the details of the upwelling process, the numerical results show that although upwelling, for small L_N, is a basin-scale wave process, partial upwelling can occur at higher L_N. Partial upwelling at large L_N is driven by general circulation and wall effects. Thus, future study needs to consider the bathymetry at the upwind end of natural systems and its effect on the structure of the flow.

Acknowledgement

The authors are grateful for the valuable comments made by the anonymous referees on an earlier version of this manuscript.

References

1. D.L. Stefanovic and H.G. Stefan, Simulation of transient cavity flows driven by buoyancy and shear. *J. Hyd. Eng.* 38 (2000) 181–195.
2. C.H. Mortimer, Water movements in lakes during summer stratification. Evidence from the temperature distribution in Windermere. *Phil. Trans. R. Soc. London* B236 (1952) 255–404.
3. R.H. Spigel and J. Imberger, The classification of mixed-layer dynamics in lakes of small to medium size. *J. Phys. Oceanogr.* 10 (1980) 1104–1121.
4. R.O.R.Y. Thompson and J. Imberger, Response of a numerical model of a stratified lake to a wind stress In: T. Carstens and T. McClimans (eds.), *Proc. 2nd Intl. Symp. Stratified Flows, Trondheim* Vol. 1 (1980) pp. 562–570.
5. S.G. Monismith, An experimental study of the upwelling response of stratified reservoirs to surface shear stress. *J. Fluid Mech.* 171 (1986) 407–854.
6. C. Stevens and J. Imberger, The initial response of a stratified lake to a surface shear stress. *J. Fluid Mech.* 312 (1996) 39–66.
7. J. Imberger and J.C. Patterson, Physical Limnology. *Adv. Appl. Mech.* 27 (1989) 303–473.
8. C. Stevens and G.A. Lawrence, Estimation of wind-forced internal seiche amplitudes in lakes and reservoirs, with data from British Columbia, Canada. *Aquatic Sciences* 59 (1997) 115–134.
9. J.A. Church and R.O.R.Y. Thompson, Cloud-in-cell and finite-difference models for a stratified lake. In: J. Noye (ed.), *Numerical Solutions of Partial Differential Equations.* North-Holland (1982) pp. 455–469.
10. R. Franke, M.A. Leschziner and W. Rodi, Numerical simulation of wind-driven turbulent flow in stratified water bodies. In: E.J. List and G.H. Jirka (eds.), *Proc. 3rd Int. Symp. Stratified Flows, Pasadena, California* (1987) pp. 993–1004.
11. C.R. Chu and C.K. Soong, Numerical simulation of wind-induced entrainment in a stably stratified water basin. *J. Hydraulic Res. IAHR* 35 (1997) 21–41.
12. C.J. Freitas, R.L. Street, A.N. Findikakis and J.R. Koseff, Numerical simulation of three-dimensional flow in a cavity. *Int. J. Num. Meth. Fluids* 5 (1985) 561–575.
13. J.R. Koseff and R.L. Street, Circulation Structure in a stratified cavity flow. *ASCE J. Hyd. Eng.* 111 (1985) 334–354.
14. B.R. Hodges Recirculation and the equilibrium displacement of the thermocline in a wind-driven stratified lake. In: G.A. Lawrence, R. Pieters and N. Yonemitsu (eds.), *Proc. 5th Int. Symp. Stratified Flows, Vancouver, British Columbia* (2000) pp. 327–330.
15. B.R. Hodges, J. Imberger, A. Saggio and K.B. Winters, Modeling basin-scale internal waves in a stratified lake. *Limnol. Oceanogr.* 45 (2000) 1603-1620.
16. S.W. Armfield, Finite-difference solution of the Navier-Stokes equations on staggered and non-staggered grids. *Comp. Fluids* 20 (1991) 1–17.
17. S.V. Patankar, *Numerical Heat Transfer and Fluid Flow.* Washington D.C./New York:Hemisphere/McGraw-Hill (1980) 197pp.
18. B.P. Leonard, A stable and accurate convective modelling procedure based on quadratic upstream interpolation. *Comput. Meth. Appl. Mech. Engng.* 19 (1979) 59–98.
19. D.W. Peaceman and H.H. Roachford, The numerical solution of parabolic and elliptic differential equations. *J. Soc. Ind. Appl. Math.* 3 (1955) 28–41.